J. Phys. Chem. A 2009, 113, 4035–4044 4035

Imaging with Mass Spectrometry: A Secondary Ion and VUV-Photoionization Study of Ion-Sputtered Atoms and Clusters from GaAs and Au[†]

Lynelle K. Takahashi,[‡,§] Jia Zhou,[‡] Kevin R. Wilson,[‡] Stephen R. Leone,[‡,§,||] and Musahid Ahmed*[,‡]

Chemical Sciences Division, Lawrence Berkeley National Laboratory, Berkeley, California 94720, and Department of Chemistry, and Department of Physics, University of California at Berkeley, Berkeley, California 94720

Received: November 26, 2008; Revised Manuscript Received: January 16, 2009

A new mass spectrometry surface imaging method is presented in which ion-sputtered neutrals are postionized by wavelength-tunable vacuum ultraviolet (VUV) light from a synchrotron source. Mass spectra and signal counts of the photoionized neutrals from GaAs (100) and Au are compared to those of the secondary ions. While clusters larger than dimers are more efficiently detected as secondary ions, certain species, such as As_2, Au, and Au_2, are more efficiently detected through the neutral channel. Continuously tuning the photon wavelength allows photoionization efficiency (PIE) curves to be obtained for sputtered As_m ($m = 1,2$) and Au_n ($n = 1-4$). From the observed ionization thresholds, sputtered neutral As and Au show no clear evidence of electronic excitation, while neutral clusters have photoionization onsets shifted to lower energies by ~0.3 eV. These shifts are attributed to unresolved vibrational and rotational excitations. High-spatial resolution chemical imaging with synchrotron VUV postionization is demonstrated at two different photon energies using a copper TEM grid embedded in indium. The resulting images are used to illustrate the use of tunable VUV light for verifying mass peak assignments by exploiting the unique wavelength-dependent PIE of each sputtered neutral species. This capability is valuable for identifying compounds when imaging chemically complex systems with mass spectrometry-based techniques.

Introduction

There is enormous interest in understanding how the surfaces of nanoparticles, both inorganic and biological, influence their chemistry. The composition of nanometer-sized aerosol surfaces plays critical roles in both the radiative balance and the chemistry of the troposphere.[1] Surfaces are also critical determinants in the structure and dynamics at boundaries of different cellular structures.[2] Developing new microscopies to detect and identify molecules with high spatial resolution will clearly allow the study of more complex nanoscale chemistry. Here, we present a technique to perform chemical imaging on surfaces using a novel mass spectrometry method, wherein ion-sputtered neutrals are photoionized with high fluxes of tunable-wavelength synchrotron VUV light. Traditional electron and optical-based imaging techniques generally lack sufficient chemical specificity at the molecular level for understanding the complex chemical systems prevalent in nature. Mass spectrometric imaging using an ion nanoprobe offers a solution to this long-standing problem in the imaging community, allowing the localization of specific chemical species on length scales of 100 nm or less. Until now, either the secondary ions (secondary ion mass spectrometry or SIMS) or the laser postionized ion-sputtered neutral species (secondary neutral mass spectrometry or SNMS) have been detected, the latter often involving harsh multiphoton ionization conditions. Here, we report the gentle, single photon ionization imaging of ion-nanoprobe-sputtered neutrals by synchrotron VUV light.

Ion sputtering has found extensive application in the physical modification of material surfaces,[3] and it is the key process behind SIMS and SNMS. As such, ion sputtering has been the subject of many experiments and extensive molecular dynamics simulations,[4] but much of the detailed physics of the sputtering process is still not well understood. Upon surface bombardment with keV atomic or cluster ion projectiles, a series of rapid collision cascades[5] is generated within the solid, resulting in the localized ejection of surface species in neutral, positive, and negative charge states. In this complex process, the translational energy from the incident primary ions can be transferred to the ejected atoms and molecules in the form of kinetic, vibrational, rotational, or electronic energy.

To image with SIMS and SNMS, an ion source is rastered across the sample, and the mass spectrum collected from each spatial pixel is used to reconstruct a complete chemical image of the analyzed surface. In SIMS, mass spectra of the sputtered secondary ions are analyzed, and in SNMS, the sputtered neutrals are postionized before extraction into a mass spectrometer. Both imaging techniques have long been utilized in the semiconductor industry, where the localized chemical distributions of various dopants can be mapped as a function of lateral position and depth within semiconducting samples.[6] More recently, SIMS has also found applications in imaging organic and biological samples. Among these advancements, Kraft et al. used SIMS to image lipid domains within prepared lipid membranes down to ~100 nm,[7] Colliver et al. used SIMS imaging to study the organism paramecium,[8] and Lechene et al. successfully used SIMS with multi-isotope imaging to map

[†] Part of the "George C. Schatz Festschrift".

* Corresponding author. Phone: (510) 486-6355. Fax: (510) 486-5311. E-mail: mahmed@lbl.gov.

[‡] Lawrence Berkeley National Laboratory.

[§] Department of Chemistry, University of California at Berkeley.

[||] Department of Physics, University of California at Berkeley.

10.1021/jp810408v CCC: $40.75 © 2009 American Chemical Society
Published on Web 02/27/2009

the fate of fixed nitrogen in host cells.[9] Furthermore, Fletcher et al. performed depth profiling experiments to generate three-dimensional chemical images of whole frog eggs,[10] and Ostowski et al. imaged the heterogeneous distribution of lipids in cell membranes of mating Tetrahymena (a protozoan).[11]

Despite these advancements, certain aspects of SIMS imaging remain problematic. One issue is that secondary ion signal intensities can vary dramatically across a single sample due to the sensitivity of ion sputter yields to the local chemical environment ("matrix effects").[12] Yields are higher and less subject to local chemical variations across a sample for secondary neutrals than for secondary ions, so SNMS has been pursued in several groups. SNMS imaging with laser postionization (PI) has been performed in the past with spatial resolutions on the order of 100 nm.[13,14] Because few tunable lasers exist in the region above 7 eV where the ionization energies of most organic molecules occur, PI experiments often employ nanosecond, picosecond, or femtosecond lasers in multiphoton ionization schemes to probe both inorganic and organic samples.[15−17] Extra internal energy deposited into sputtered molecules during such multiple photon ionization processes, however, often results in molecular fragmentation.[18] The complications introduced by fragmentation are amplified when analyzing heterogeneous samples such as biological cells, where thousands of chemical compounds are present. It is therefore necessary to study the energetics of sputtered neutral species and to devise methods to aid in the identification of mass spectral features.

One method of minimizing fragmentation is to softly ionize sputtered neutral species using threshold VUV single photon ionization.[19,20] Recently, tunable synchrotron VUV light was utilized to photoionize laser desorbed organic molecules at different photon energies and study molecular fragmentation pathways.[21] Peterson et al. found that SNMS with different postionizing VUV laser wavelengths could be used to selectively analyze classes of chemical components (organic and inorganic) within atmospheric aerosol particles.[22] Veryovkin et al. used VUV light from the Advanced Photon Source free electron laser to postionize inorganic species sputtered by noble gas primary ions,[23] but the experiments suffered from a very low repetition rate of 6 Hz and limited wavelength tunability.

In this Article, we present tunable synchrotron VUV photoionization of ion-sputtered neutrals as a method for chemically selective imaging of multicomponent samples. The features and performance of this method are compared to normal SIMS imaging. With the wavelength tunability of the synchrotron light, threshold ionization is made possible, which can minimize molecular fragmentation as compared to typical multiphoton ionization schemes used in previous PI studies. Unlike many laser PI techniques, data acquisition rates are not limited by the duty cycle of a laser, because the synchrotron's light beam is quasi-continuous. This fact allows for routine operation at 10 kHz, which is limited only by the repetition rate of the ion gun and the flight times of the postionized neutrals. Furthermore, because each chemical species has a characteristic photoionization efficiency wavelength dependence, tuning the synchrotron photon energy can provide additional information that can be used to identify chemical compounds with less ambiguity. This enhanced selectivity and the reduced imaging artifacts arising from SIMS "matrix effects" are essential for extracting useful information from heterogeneous chemical systems.

Experimental Methods

A modified commercial secondary ion mass spectrometer (TOF.SIMS 5, ION-TOF Inc.), operating under ultrahigh vacuum conditions (10^{-9} mbar, 1 mbar = 0.1 kPa), is coupled to a VUV light source on the Chemical Dynamics Beamline at the Advanced Light Source, Lawrence Berkeley National Laboratory (Figure 1). The setup utilizes a bismuth liquid metal ion gun (LMIG), mounted at 45° with respect to the sample surface normal, to deliver pulses of bismuth cluster primary ions (Bi^+, $Bi_3{}^+$, or $Bi_3{}^{2+}$) at a repetition rate of around 10 kHz. All analyses are performed using beams of a single type of bismuth cluster ion at any given time, which is selected via a time-of-flight filter within the ion gun.

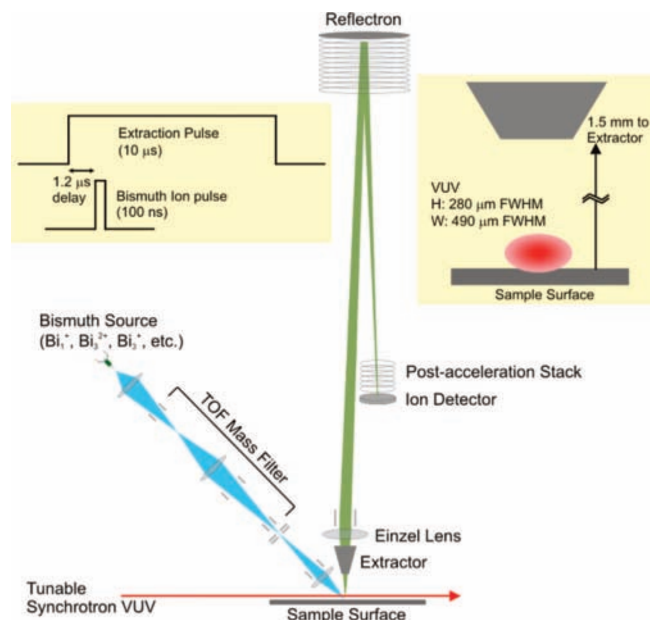

Figure 1. Schematic of the TOF.SIMS 5 setup coupled to the synchrotron VUV beamline. The bismuth primary ion beam is represented in blue, the VUV beam is indicated in red, and the path of the extracted postionized neutrals is shown in green. An outline of the extraction pulse timing with respect to the LMIG pulse (upper left) and an expanded view of the light with respect to the sample stage (upper right) are also shown.

Samples are held at ground potential, 1.5 mm away from the analyzer extraction cone. About 1 μs before each primary ion pulse impinges on the sample surface, the extraction cone is pulsed from 0 to −2000 V and is held at −2000 V for 10 μs (see Figure 1, top left for timing scheme). The positively charged secondary ions and postionized neutrals are extracted into a reflectron-type time-of-flight (TOF) mass spectrometer with a 2 m long path length and are detected and recorded through the TOF.SIMS 5 computer software.

The optimal analyzer conditions for the detection of secondary ions and postionized neutrals are different due to the different extraction voltages that the two ion populations experience in the extraction scheme described above. Secondary ions are extracted immediately upon their formation at the sample surface and are therefore accelerated through the full −2000 V between the sample surface and the extractor cone. Postionized neutrals, on the other hand, accelerate through a range of extraction voltages depending on the height above the surface at which they are ionized. This spread in extraction potential results in a broader range of paths through the analyzer for the postionized neutrals than for the secondary ions, which prompted the removal and enlargement of several apertures along the flight path of the original TOF.SIMS 5 instrument. Because the postionized neutrals experience lowered extraction potentials due to their formation a finite distance away from the sample surface, they possess correspondingly lowered kinetic energies

as they travel through the TOF analyzer. This results in lower optimal voltages for the Einzel lens for PI detection (4600 V as compared to 4840 V for optimized SIMS; see Figure 1 for an overview of analyzer components). The voltage applied to the last reflector plate within the analyzer is also lower for optimized PI conditions (−20 V as compared to +20 V for optimized SIMS). Optimized PI settings are used for all data sets utilized in the presented PI spectra and PIE curves. Optimized SIMS settings are only used for data sets used to make direct comparisons between PI and SIMS.

The mass spectra and PIE curves in this Article are measured with the LMIG in the highest-current mode at 25 keV (doubly charged species are emitted at 50 keV), using a pulsed ion beam of Bi^+, Bi_3^+, or Bi_3^{2+} (100 ns pulse length, corresponding to approximately 9.1, 2.5, and 2.2 pA current, respectively, at 10 kHz) with a ~5 μm diameter spot size. The images presented in this Article are acquired using two high-spatial resolution settings of the LMIG, with spot sizes of ~100 nm (1000 ns pulse widths) and ~250 nm (800 ns pulse widths). Long LMIG pulse widths are used for imaging to minimize data collection time, although the use of shorter pulse widths is possible.

The beamline, described in detail elsewhere,[24] uses an undulator to generate wavelength-tunable, quasi-continuous (500 MHz) VUV light in the region from 7.5 to 25 eV. The spectral resolution of the light used in this work is determined to be ~0.35 eV by measuring the spectral fwhm of the autoionizing resonance of ion-sputtered silicon atoms. The light from the undulator is reflected by three mirrors before passing through the TOF.SIMS 5. The first two mirrors focus the VUV light to the center of a differentially pumped gas filter to remove higher energy harmonic radiation. Argon is used in the gas filter for the present experiments, filtering out photons with energies above the Ar ionization threshold of 15.76 eV. After the gas filter, the light is again reflected and focused by a gold-coated toroidal mirror, which delivers $10^{15}-10^{16}$ photons/s (at 400 mA synchrotron current) with a spot size of approximately 280 μm (vertical) × 490 μm (horizontal) to the terminal where the TOF.SIMS 5 instrument is situated. This last mirror is controlled by two motorized stages, allowing the light position to be finely adjusted in the ion extraction area.

Photon flux curves as a function of energy are determined using a NIST-calibrated photodiode (SXUV-100, International Radiation Detectors) and a picoammeter (486 picoammeter, Keithley) attached to the light exit port. All energy spectra are normalized to the measured flux curve. Corrections are also made to the photon energy scans presented in this Article to account for the exponential decay of the overall photon flux, which decays with the lifetime of the electrons in the synchrotron storage ring, although the overall effect is minimal for the short time scans reported here. Corrections are not applied for height changes induced in the analyzed sample area by ion-sputtering.

Au (Alfa Aesar, 0.1 mm thick, 99.95%) and standard GaAs (100) samples are clamped onto the edge of an aluminum top-mount sample holder closest to the incoming photon beam, allowing the synchrotron light to pass as close to the sample as possible. A VUV-induced current can always be measured from the sample stage, indicating that a part of the near-Gaussian "tail" of the photon beam spatial profile impinges on the sample. This grazing light configuration is used for optimal overlap of the photon beam with the sputtered neutral plume. For both samples, 500 μm × 500 μm regions are scanned six times with a DC beam of bismuth ions (current ~15 nA, all cluster-ion species of bismuth) prior to analysis to ensure surface cleanliness and spectral reproducibility, although only the central 100 μm × 100 μm area is analyzed for the spectra and PIE curves presented here. This smaller area is analyzed with 500 scans using a 16 × 16 pixel raster for each data set. Sample analysis is conducted at room temperature (~300 K). Three data sets are taken for each PI data point, each measured under the optimal analyzer conditions for PI: one measuring the signal directly from the ion gun (SIMS background signal), one measuring the synchrotron-ionized background signal, and one measuring the signal arising from the LMIG and the synchrotron together. SIMS background and synchrotron background scans are subtracted from the signal arising from the LMIG and synchrotron together to yield the PI spectra.

To demonstrate high-spatial resolution imaging with VUV PI, a copper TEM grid embedded in indium is imaged. The sample is prepared on a stainless steel substrate, onto which a piece of flattened indium wire is placed. The copper grid is put on top of the flattened indium and is subsequently flattened between another stainless steel substrate with pliers. The top stainless steel piece is then removed to reveal the copper grid pushed into the indium metal. As with the GaAs and Au samples, the grid sample is mounted on the edge of the aluminum top-mount sample holder closest to the incoming light and is subjected to six DC scans from the LMIG prior to analysis.

Results and Discussion

TOF Analyzer Transmission. The analyzer transmission efficiency is estimated by leaking 1.0×10^{-8} mbar of Xe into the main chamber with a base pressure of 4.1×10^{-9} mbar. The gas is ionized with 14 eV photons. At 14 eV photon energy, the expected number of Xe counts per second, S, is given by:

$$S \approx \sigma F N \alpha \tag{1}$$

where σ is the photoionization cross section of Xe at 14 eV, F is the photon flux at 14 eV, N is the number of Xe atoms in the ionization volume (assumed to be constant), and α is the fraction of total ions formed that are extracted by the analyzer pulse. At 14 eV, Xe has an ionization cross section of 50 Mb (1 Mb = 1×10^{-18} cm^2),[25] and the average photon flux is measured to be 1.8×10^{18} photons/(cm^2 s). Spectra are taken using 10 μs analyzer extraction pulses at 10 kHz, although ionization of Xe occurs continuously. Assuming that the equivalent of 10 μs of ionized Xe resides in the extracted volume at the time of the extraction pulse, α is 0.2 (all ions formed in 10 μs before the pulse + all ions formed during the 10 μs extraction pulse are extracted). If the sampled ionization volume is approximated by the dimensions of the light beam cross section and the 1 mm diameter opening of the analyzer extractor cone, then at the given pressure, about 1.97×10^4 Xe atoms are present in the sampled ionization volume, yielding $S = 3.59 \times 10^5$ counts per second. Experimental measurements result in 3.00×10^4 counts per second for all isotopes of Xe, corresponding to a detection efficiency of ~8%.

With the calculated detection efficiency through the analyzer, measured signal intensities, LMIG current, photon flux, and ionization cross sections, approximate neutral sputter yields can be deduced. For the discussion here, Zn is considered because its absolute photoionization cross section is known.[26] If 8% detection efficiency is assumed for neutrals desorbed from a Zn sample, then at a photon energy of 11.9 eV the number of Zn atoms that are sputtered per second, $\tilde{N}$, can be calculated

using a formula very similar to eq 1:

$$\tilde{N} = \frac{Z}{0.08\tilde{\sigma}\tilde{F}\tilde{\tau}} \qquad (2)$$

where 0.08 is the detection efficiency, $\tilde{\sigma}$ is the photoionization cross section of Zn at 11.9 eV, $\tilde{F}$ is the photon flux at 11.9 eV, Z is the number of Zn PI counts observed per second, and $\tilde{\tau}$ is the average time that each of the neutrals spend in the VUV beam path. At 11.9 eV, Zn has an approximate cross section of 150 Mb,[26] and the average photon flux is measured to be approximately 1.77×10^{18} photons/(cm^2 s). With the vertical extent of the light beam measured to be 280 μm and assuming a typical kinetic energy of 1 eV[27] for the sputtered Zn, $\tilde{\tau}$ is 0.16 μs. Experimental measurements obtain 1.21×10^4 Zn PI counts per second for all isotopes of Zn upon bombardment with Bi^+ primary ions. Inputting these values into eq 2 yields 3.6×10^9 sputtered neutral Zn atoms per second, which, with 9.1 pA of Bi^+ beam current, corresponds to an approximate neutral sputter yield of 62.7 Zn atoms per incident Bi^+ primary ion. This value is in good agreement with the prediction of 83.8 sputtered Zn per Bi^+ obtained using the semiempirical Yamamura formula[28,29] for Bi^+ primary ions at 45° incidence. A similar analysis of Zn PI signal resulting from Bi_3^+ bombardment gives a 8.5 times yield enhancement per incident ion as compared to Bi^+. Although the change in the sputter yield in going from atomic to cluster primary ions depends on the specific projectile−sample combination,[30] the enhanced sputter yield with the use of cluster projectile ions is also generally observed for other systems.[30,31]

Synchrotron VUV Postionization and SIMS. Several sample substrates (Ag, Cu, Si, In, Ge, Pt, and Zn) are analyzed with the present experimental arrangement, but only the results obtained for GaAs and Au are presented in detail here. GaAs and Au are chosen because both yield VUV PI spectra with relatively high signal intensities for dimers and larger clusters. The observation of clusters is desirable because clusters, unlike atoms, can possess vibrational and rotational excitations. Furthermore, GaAs and Au are discussed because they yield neutral clusters (As_2, Au_2, and Au_4) that exhibit ionization thresholds well within our available photon range. This allows adequate baseline counts to be collected so that ionization thresholds can be obtained from the PIE curves (discussed later).

SIMS and neutral PI mass spectra using 100 ns Bi_3^+ primary ion beams and 10.5 eV photons are collected from GaAs and Au and are compared in Figure 2. 10.5 eV is chosen because it yields the highest Au_2 and As_2 PI signals and because previous laser PI studies over GaAs have been done at 10.5 eV.[19] For a meaningful comparison of the spectra in Figure 2, the SIMS and PI spectra are collected under the optimum analyzer conditions for each. The corresponding signal counts for the data sets used in Figure 2 are summarized in Table 1. From the table, it is seen that each PI peak has different SIMS and synchrotron background levels. For the particular case of Au_2 and 10.5 eV ionizing photons, the PI signal intensity dominates the background signals from both sources and is reproducible to within 1%.

From the comparison of SIMS and PI spectra in Figure 2, it is clear that SIMS has higher signal intensities for larger clusters, although the signal intensities of SIMS and PI for Au and As are comparable. The integrated PI signal intensities for Au_2 and As_2 at 10.5 eV, however, are factors of 6 and 9 higher than their respective SIMS peaks. The prominence of these neutral dimers as compared to either neutral Ga or As is likely due to

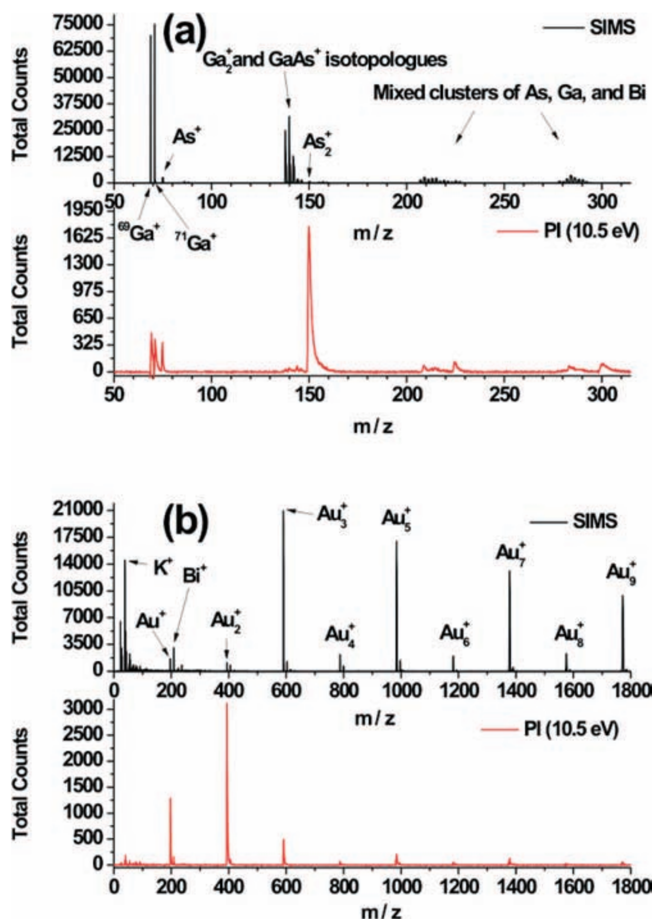

Figure 2. SIMS and PI spectra obtained over (a) GaAs and (b) Au using a Bi_3^+ primary ion beam. The PI spectra for both surfaces are collected using 10.5 eV photons, the photon energy with maximal signal intensity for As_2 and Au_2. SIMS and PI spectra presented here are taken under their respective optimal analyzer settings.

a combination of a large sputter yield and ionization probability and illustrates the complementary nature of the SIMS and VUV PI techniques. It should be noted that the observed relative intensities of the postionized neutral clusters in Figure 2 do not reflect the absolute population distribution within the neutral plume. Unlike most laser PI experiments, the relative intensities observed with the current experiments are strong functions of the species-specific ionization cross sections because the synchrotron does not saturate the photoionization process.

In the SIMS spectra for the Au surface (Figure 2b, top), there is a cluster of peaks at low m/z resulting from surface contaminants. Most notable is the large peak from potassium at m/z ∼39. Although potassium is presumably a small component on the Au surface, the K^+ peak intensity is comparable to those of the strongest gold cluster peaks due to the ease with which it forms secondary ions. These low m/z trace contaminants are not present in the PI spectra. In fact, the small peaks at low m/z in the PI spectra (Figure 2b, bottom) are purely a result of incomplete background subtraction resulting from the scan-to-scan variation of the SIMS intensity. This conclusion is supported by the narrow widths of the low m/z peaks (PI peak widths are discussed below).

Figure 3 shows an expanded view of the PI spectra of Figure 2. The PI peaks exhibit a sharp Gaussian-like leading edge and a broader, Lorentzian-like tail toward later times. As_2 (m/z = 149.84) has a PI peak with $m/\Delta m \approx 100$, which under the conditions used in this experiment is comparable to the $m/\Delta m \approx 200$ for the corresponding optimized SIMS As_2 peak. SIMS

TABLE 1: Counts for Optimized SIMS, Compared to the Counts for the Synchrotron Background, SIMS Background, Synchrotron + LMIG Signals, and PI Signals for Select Atoms and Clusters at 10.5 eV (Corresponding Mass Spectra are Shown in Figure 2)[a]

	optimized for SIMS	optimized for PI			
atom or cluster	SIMS	synchrotron background	SIMS background	synchrotron + LMIG	PI[b]
^{69}Ga	1.27×10^5	360	6.52×10^4	7.24×10^4	6.84×10^3
As	2.35×10^4	260	39	4.63×10^3	4.33×10^3
As_2	5.62×10^3	610	79	5.09×10^4	5.02×10^4
Au	8.09×10^3	160	570	1.14×10^4	1.06×10^4
Au_2	5.66×10^3	75	170	3.47×10^4	3.45×10^4
Au_3	8.36×10^4	19	3.58×10^3	7.62×10^3	4.03×10^3
Au_4	1.09×10^4	14	42	629	570

[a] Signals are collected over a 100 μm × 100 μm area with a 16 × 16 pixel raster over 500 scans (∼13−19 s; longer times used for the large Au clusters). [b] PI signal counts are the final result after subtraction of "SIMS background" (SIMS under optimal PI analyzer conditions) and "synchrotron background" from the signals resulting from the "synchrotron + LMIG" together.

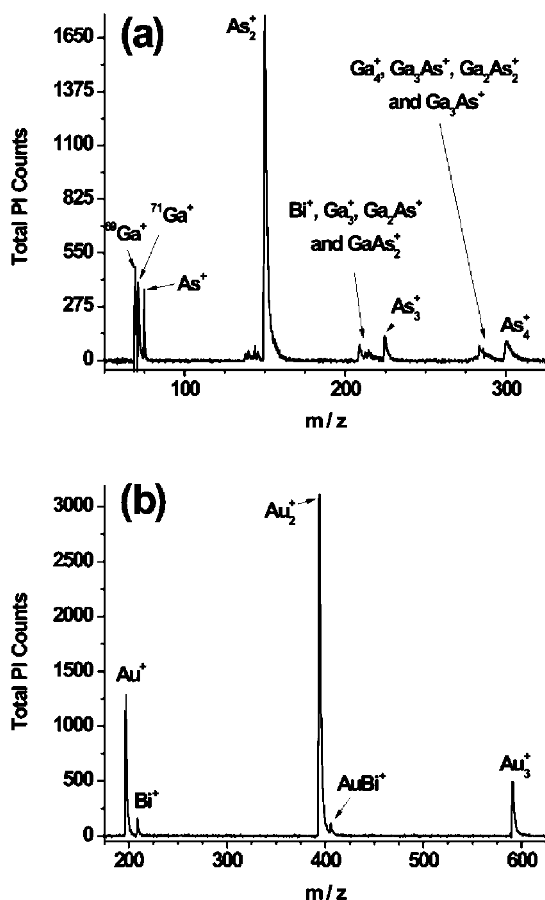

Figure 3. Expanded view of the PI spectra shown in Figure 2 over (a) GaAs (100) and (b) Au obtained with 10.5 eV photons and 100 ns pulses of Bi_3^+ primary ions.

peak widths scale with LMIG pulse length, so SIMS mass resolution can be improved by shortening the LMIG pulse length. The PI peakwidths, on the other hand, do not scale closely with LMIG pulse width for short pulses below 100 ns, so mass resolution cannot be improved using the same method. This behavior may be attributed to the quasi-continuous photoionization and the finite vertical dimension of the photon beam. Because of these two factors, neutrals are ionized (and extracted) at different times and can experience a range of extraction voltages. While the reflectron compensates somewhat for the second effect, it cannot compensate for the spread in the "time-of-birth" of the postions. Despite this, it is possible to narrow PI peaks by a factor of ∼3 by delaying the analyzer extraction pulse with respect to the primary ion pulse (data not shown). For the data presented in this Article, however, long LMIG pulse lengths of 100 ns are used so that SIMS and PI peaks have comparable width, making PI signals easier to identify.

So far, SIMS and SNMS are shown to be complementary techniques that can yield different information for the analyzed surface. While SIMS is typically more sensitive than synchrotron VUV PI for the larger clusters, synchrotron VUV PI yields comparable signals for smaller species like Au, Au_2, As, and As_2 and is not subject to the nonrepresentative high peak intensities of low *m/z* trace contaminants. Observed PI peaks are generally broader than SIMS peaks, but can be narrowed by delaying the application of the extraction voltage. Not yet discussed are the additional advantages of synchrotron VUV PI as compared to SIMS and conventional laser PI due to the unique wavelength tunability of the synchrotron. One such advantage is the capability to study the energetics of sputtered neutrals, as is discussed in the following section.

Photoionization Efficiency Curves. To investigate the internal energies of sputtered neutral species, PIE curves are obtained for sputtered neutrals from GaAs (100) and Au by varying the photon energy in 0.15 eV steps. Wucher et al.[32] previously collected PIE curves using single photon laser ionization to illustrate the high internal temperatures of ion-sputtered indium clusters as compared to cold clusters from a supersonic nozzle expansion. In the present experiment, sets of three PIE scans for each substrate are taken over the same area in succession with each of the primary ion beams (Bi^+, Bi_3^+, and Bi_3^{2+}) to determine whether neutrals sputtered by different primary ions have significantly different internal energies. For scans from GaAs, the photon energy range from 7.5 to 14 eV is scanned; for scans from gold, the photon energy is varied from 7.5 to 12 eV.

PIE curves can provide information about the internal excitation of the sputtered neutral species from the surface. According to the Franck−Condon principle, the most probable electronic and vibrational transition will be that with the least geometry change (vertical transitions). If the neutrals contain internal energy, then there is a distribution of initial state energies and geometries, which may increase the energy range of the allowed vertical transitions. Thus, internal energy may broaden and change the shape of the PIE curve ionization onset[33] in addition to lowering the energy needed for ionization to occur. Figure 4 compares the As_2 PIE curves resulting from Bi_3^+, Bi^+, and Bi_3^{2+} primary ion bombardment. As_2 has the highest maximum PI intensity and signal-to-noise of all species analyzed from GaAs, possibly due to the particular stability of the neutral As_2 molecule, which is characteristic of group 5A diatomics.

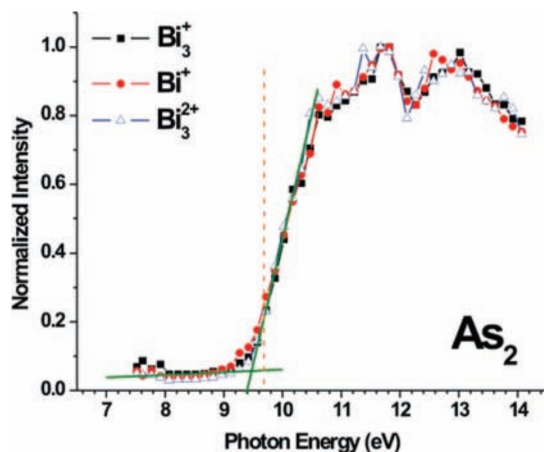

Figure 4. PIE curves for As_2 resulting from the three primary ion beams indicated in the graph legend. The literature experimental adiabatic ionization energy from Table 2 is indicated by the vertical orange dashed line, and the extrapolation lines used to determine the ionization threshold energy are indicated in green.

TABLE 2: As_m ($m = 1, 2$) Observed Ionization Thresholds, Compared to Previous Experimental Ionization Energies[a]

As_m	this work	literature ionization energy
$m = 1$	9.62 ± 0.18	9.79[b]
$m = 2$	9.42 ± 0.18	9.69[c,d]

[a] All energies are in eV. [b] Evaluated arc spectrum from ref 36. [c] Photoionization from ref 34. [d] Adiabatic ionization energy.

No distinctive differences are visible among the three PIE curves obtained for As_2 with the different primary ion beams, nor are any significant differences seen for other sputtered species from the GaAs and Au surfaces; hence, the set of three PIE scans is only shown for As_2.

The ionization onset slope and low-photon energy baseline of the As_2 PIE curves are linearly extrapolated (Figure 4, green lines), and the energy at the intersection of the lines is taken to be the threshold ionization energy. Small features in the low energy regions (at and below approximately 7.9 eV) of the PIEs likely arise from the residual harmonic radiation of the undulator passing through the argon gas filter. These data points are therefore excluded from the fits for the extrapolation lines used for the baselines of the PIE curves. This linear extrapolation method yields the same As_2 ionization threshold energy (9.42 $\pm$ 0.18 eV) for each of the three primary ion beams. This value is compared to literature experimental and theoretical ionization energies in Table 2, where it can be seen that the observed ionization threshold lies 0.27 eV lower than the adiabatic ionization evaluated by Yoo et al.[34] This 0.27 eV difference is suggestive of vibrational excitation of the sputtered As_2. Because the lowest-lying As_2 electronically excited state lies nearly 1.8 eV above the ground electronic state[35] and this is not observed in the PIE curve, we conclude that electronic excitation for sputtered neutral As_2 is likely insignificant.

Similar analysis of the PIE onset for As (Figure 5) yields an ionization onset of 9.62 ± 0.18 eV for all three incident primary ion beams. This value agrees with literature values for the As ionization energy[36] within experimental uncertainty. Because As atoms cannot undergo vibrational or rotational excitation, the only excitation possible is electronic; however, the lowest As excited electronic state lies 1.3 eV above the ground electronic state.[37] Because no features are observed in the PIE 1.3 eV below the ionization threshold, electronic excitation appears not to play a role in the sputtered neutral As.

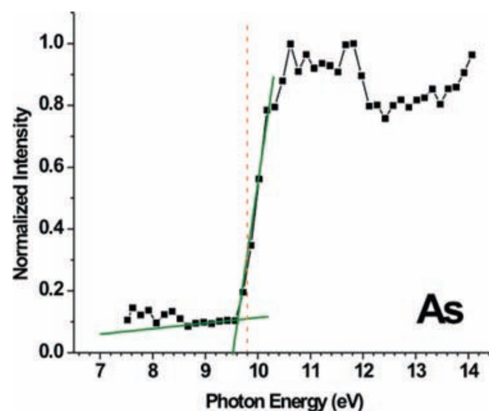

Figure 5. PIE curve for As from Bi_3^+ primary ion bombardment. The vertical orange dashed lines represent literature experimental adiabatic ionization energy taken from Table 2, and the green lines represent the extrapolation lines used to determine the ionization threshold.

As was noted in the previous section, all PI mass peaks that are observed in this experiment, including that for As_2, have a characteristic shape and finite width, with a sharp Gaussian-like rising edge and a Lorentzian-like tail toward later arrival times (see Figure 3a,b). Because of the particularly strong signal levels for As_2, PIE curves can be reconstructed for both the rising edge and the trailing tail portions of the As_2 mass peak resulting from Bi_3^+ bombardment; however, only minor differences (within the experimental resolution) are observed for the obtained ionization threshold values. Similar observations are made when a delay (up to 0.6 μs) is applied between the LMIG and analyzer extraction pulses. In these delayed extraction experiments, no differences in the resulting PIE curve shape or onset values are observed. These observations indicate that there are minimal differences in the internal excitation of sputtered neutrals leaving the surface with different velocities or at different times for these systems.

Extensive gold cluster ion formation is seen upon ion bombardment (Figure 2b, top), and neutral clusters are also produced, as they have been observed on other metal substrates.[38] PIE curves are obtained for gold clusters with up to four Au atoms.

The PIE for Au exhibits a sharp rise (Figure 6a). Linear extrapolation of the sharp rise to the baseline yields a threshold ionization energy of 9.22 ± 0.18 eV, which is in good agreement with literature values for the ionization energy (see Table 3). Au can only possess electronic excitations, but the lowest electronically excited state lies over 1.1 eV above the ground state.[39] The lack of features in the Au PIE 1.1 eV below the ionization threshold suggests the absence of electronic excitation.

Au_2 has the highest maximum PI intensity of all clusters sputtered from the Au surface. Analysis of the Au_2 PIE curve (Figure 6b) yields an ionization threshold of 8.82 ± 0.18 eV. This value for the dimer ionization threshold is 0.34 eV lower than the adiabatic ionization energy measured by charge-transfer bracketing and FTICR-MS,[40] indicating that neutral Au_2 leaves the surface with significant amounts of internal energy. In general, these excitations may be rotational, vibrational, or electronic in nature; however, the first excited electronic state for Au_2 lies 1.9 eV above the ground state.[41] Because there are no observable features in the PIE curve 1.9 eV below the ionization threshold, electronic excitation in ion-sputtered neutral Au_2 appears to be negligible.

The Au_3 PIE (Figure 6c) has a more gradual slope at the ionization threshold as compared to the onsets for the monomer,

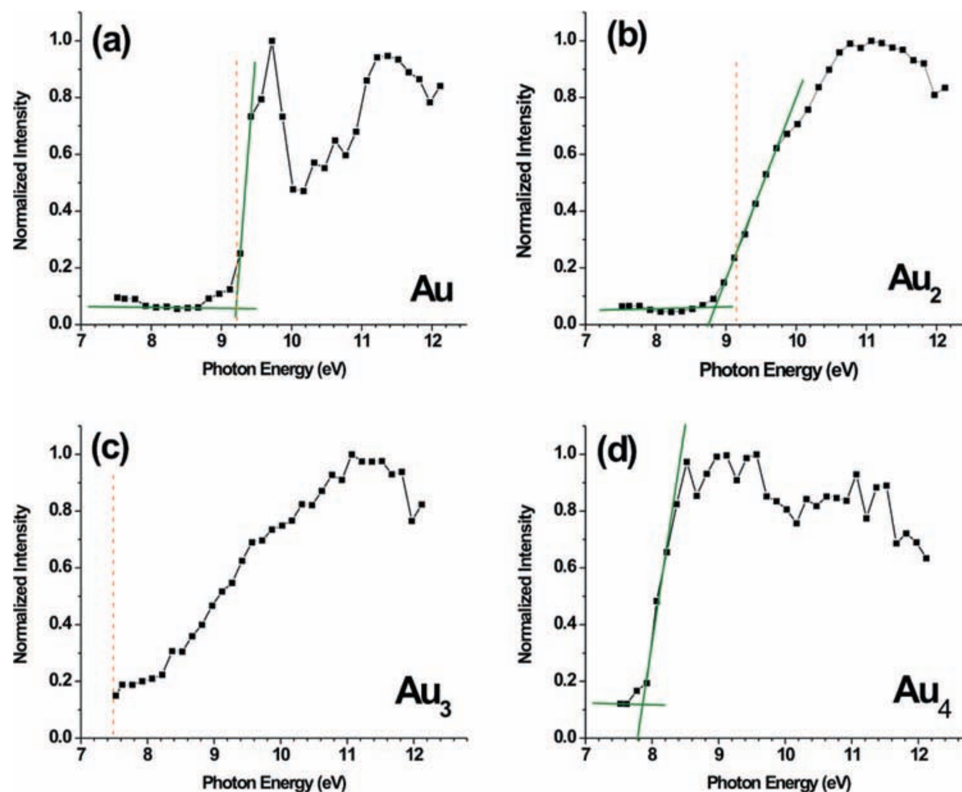

Figure 6. PIE curves for (a) Au, (b) Au_2, (c) Au_3, and (d) Au_4 from Bi_3^+ primary ion bombardment. The green lines are the extrapolation lines used to evaluate the ionization threshold values. The literature experimental adiabatic ionization energies taken from Table 3 are indicated by vertical orange dashed lines, when available.

TABLE 3: Au_n (n = 1, 2, 3, 4) Observed Ionization Thresholds, Compared to Corresponding Previous Experimental and Theoretical Values for the Ionization Energies[a]

Au_n	this work	literature experimental	literature theoretical
$n = 1$	9.22 ± 0.18	9.23;[b,c] 9.26[d]	9.78[e]
$n = 2$	8.82 ± 0.18	9.50;[b,f] 9.16[d,g]	9.84;[e,f] 9.81[e,g]
$n = 3$	~7.5	7.50;[b,f] 7.27[d,g]	linear geometry: 9.05;[e,f] 7.30[e,g] triangular geometry: 7.32;[e,f] 7.30;[e,g] 7.21[h,f]
$n = 4$	7.82 ± 0.18	8.60[b,f]	8.37;[e,f] 8.34;[e,g] 8.24[g,i]

[a] All energies are in eV. [b] Electron impact from ref 44. [c] Evaluated arc spectrum from ref 47. [d] Charge-transfer bracketing and FTICR-MS from ref 40. [e] Reference 43. [f] Vertical ionization energy. [g] Adiabatic ionization energy. [h] Reference 42. [i] Reference 48.

dimer, and tetramer. This slow rise may be due to the contributions from two low-lying geometries of the neutral trimer (linear and triangular) that have been calculated to lie within 0.02 eV[42] to 0.04 eV[43] of each other. With this small energy difference, it seems likely that both isomer structures would be populated within the sputtered neutral plume. The linear and triangular structures both have calculated adiabatic ionization energies of 7.3 eV; however, their vertical ionization energies are 9.05 and 7.32 eV, respectively.[43] This indicates that the linear isomer will have a gradual PIE onset due to poor Franck−Condon overlap, in addition to broadening from thermal vibrations in the neutral cluster. While this can explain the slow ionization onset, the proximity of the ionization threshold to the lowest accessible photon energy of 7.5 eV prevents the accurate determination of the baseline and thus does not allow us to constrain the ionization threshold above or below 7.5 eV.

Analogous analysis of the Au_4 PIE (Figure 6d) yields an ionization threshold of 7.82 ± 0.18 eV, which is 0.78 eV below literature values for the vertical ionization energy for Au_4.[44] Like the trimer, the tetramer has various energetically low-lying structural isomers that have been calculated, including the planar rhombus and the planar "Y" shape that lie within 0.21 eV of each other.[43] In another study, Kim et al. calculates the linear structure for the neutral to be 0.39 eV higher in energy than a two-dimensional rhombus structure.[42] These differences are somewhat larger than the aforementioned energy differences calculated between the linear and triangular trimer isomers, implying that the different tetramer isomers are less likely populated. From the sharp rise of the Au_4 PIE, there appears to be a good Franck−Condon overlap of the neutral and cation tetramer geometries, which is supported by the similar values for the rhombic Au_4 vertical and adiabatic ionization energies calculated by Wang et al.[43]

The photoionization thresholds obtained in this experiment for neutral atoms sputtered from both GaAs and Au agree with literature experimental values, while the ionization thresholds observed for ion sputtered neutral clusters (see Tables 2 and 3) exhibit ~0.3 eV shifts to lower energies with respect to their literature adiabatic ionization energies. For Au_3 and Au_4, low-lying isomers and the degree of Franck−Condon overlap between the neutral and cation geometries may play a role in the ionization onset slope in the PIE curve; however, there are no clear signs of direct electronic excitation. It is likely that the observed shifts in ionization energy are due to the unresolved vibrational and rotational excitations within the neutral clusters. This view is supported by previous work, where spectral fitting

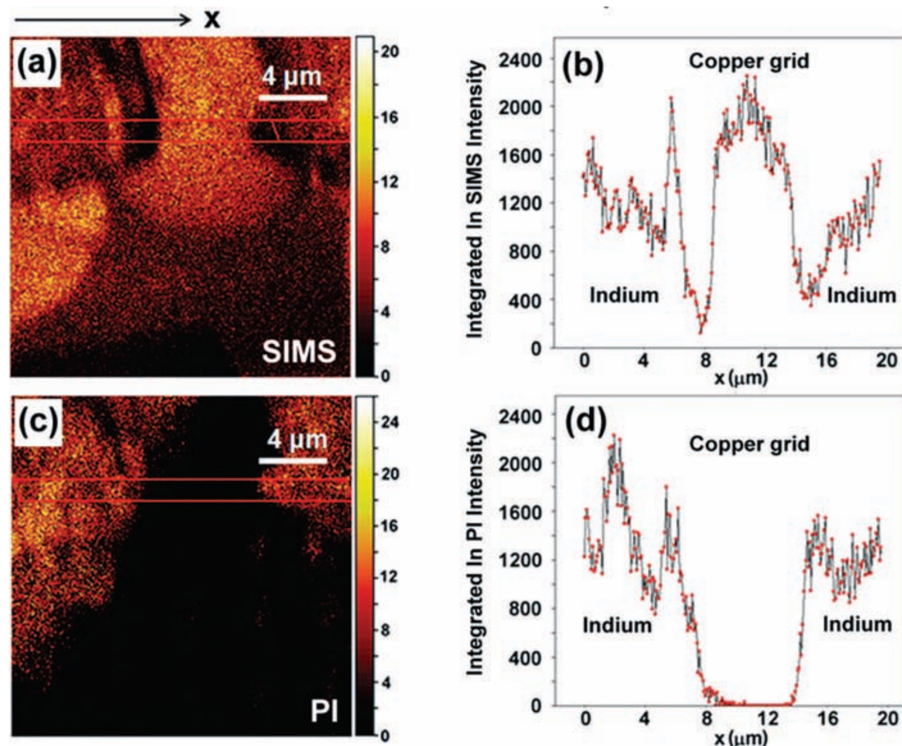

Figure 7. (a) SIMS indium image over a 20 μm × 20 μm area, at a corner of the square copper TEM grid. (b) Integrated line scan of the red selection of (a) as a function of *x*. (c) Corresponding indium PI image taken at 7.5 eV photon energy, and (d) the integrated line scan resulting from the same area selection in red for the PI image. The color scale bars to the right of (a) and (c) indicate the indium counts per pixel. Images are collected using Bi_3^+ pulse lengths of 1000 ns and a spot size of ~100 nm (256 × 256 raster, 130 scans, 852 s per data set).

yielded vibrational temperatures of 2700 K and rotational temperatures of 6700 K for sputtered silver dimers.[45]

Wavelength tunable synchrotron radiation provides a convenient means of generating PIE curves that can be used to study the internal excitations in ion-sputtered neutrals. Such quantitative understanding of the internal energies of ion-sputtered surface species is important for molecular imaging with techniques like SIMS and SNMS, in which minimization of fragmentation and sample damage is desirable; however, the wavelength tunability of the synchrotron can also be used to verify mass spectral assignments. The added selectivity of synchrotron VUV PI and its application to chemical imaging is described in the following section.

Applications to Chemical Imaging. Figure 7 shows the indium SIMS and PI images of a 20 μm × 20 μm region of a copper grid pressed into a flattened indium wire (an expanded view of the grid is shown in Figure 8). The images in Figure 7 are accumulated over 130 scans with a 256 × 256 pixel raster over 852 s with ~100 nm Bi_3^+ primary ion spot size and 1000 ns pulse lengths. From the SIMS image of indium in Figure 7a, the corner of a grid square is visible, but the indium SIMS intensity distribution is misleading. A line scan of the area selected in red across the copper gridline (Figure 7b) shows that the SIMS indium signal is actually higher in the regions of the copper grid, where a minimum in intensity would be expected from abundance arguments. This observation is likely due to the enhancement of indium secondary ion formation atop the copper grid substrate (a matrix effect). In contrast, the imaged indium PI intensity distribution (Figure 7c) collected using 7.5 eV photons over the same area reflects the expected composition of the surface. An indium PI linescan of the same selected area, shown in Figure 7d, illustrates that the indium PI signal intensity over the copper grid is lower than that over the pure indium metal. This observation reflects the much smaller

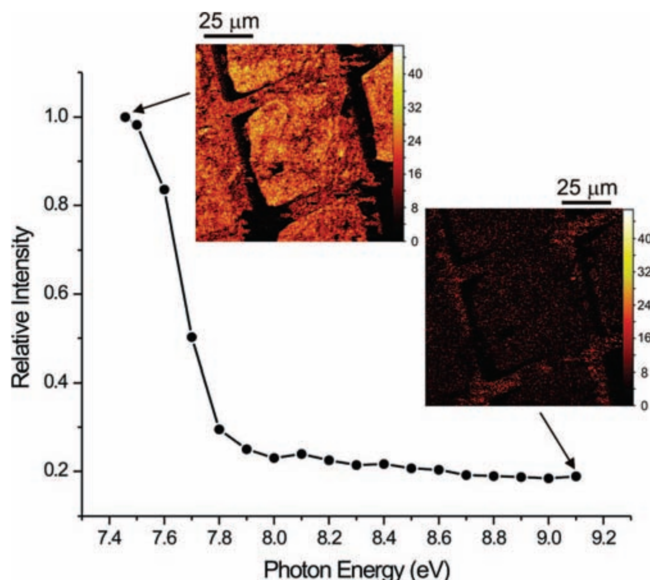

Figure 8. PI image of indium collected using 7.5 eV photons and 9.1 eV photons overlaid on their respective regions of the indium PIE curve (0.1 eV steps, 7.5−9.1 eV). Images are collected using a ~250 nm Bi_3^+ primary ion beam spot size with 800 ns pulse lengths and reflect a 100 μm × 100 μm area of the square copper TEM grid on indium (256 × 256 pixel raster, 21 scans, 550 s per data set).

effect that the local chemical environment has on the neutral desorption yields as compared to the ionization−desorption yields of the secondary ions. PI images of copper and the indium−copper heterodimer (both collected using 9.1 eV photons, not shown) of the same sample area also reflect the expected signal intensity distributions, with copper localized primarily over the copper grid line (the dark region in the indium PI image of Figure 7c), and indium−copper localized primarily

on the apparent bright spots on the copper grid in Figure 7a, where the more pliable indium smeared onto the grid. Thus, due to greatly reduced imaging artifacts from matrix effects, imaging with PI helps data interpretation even for simple chemical systems.

In addition to yielding images that more accurately reflect the chemical composition of the surface, single photon PI with tunable synchrotron VUV radiation permits more conclusive identification of chemicals by revealing differences in photoionization cross sections as well as *m/z*. In this case of the copper grid on indium, the sample's mass spectrum is relatively simple, containing only two main constituents. Even so, copper and indium PI signals behave differently at the two photon energies investigated (7.5 and 9.1 eV), in accord with their photoionization cross sections.

Indium has several autoionizing resonances near 7.5 eV[46] and can therefore be imaged well using 7.5 eV photons. Figure 8 shows the 7.5 eV PI image of indium on the left, overlaid with the indium PIE curve. In this expanded view, one may note that the indium PI signal levels fluctuate over different regions of the copper grid due to the nonuniform smearing of indium over the grid lines; however, the maximal indium PI intensities appear over the indium metal. At 9.1 eV, the indium photoionization cross section is smaller, and this fact is reflected by lower indium PI signal intensities across the image shown on the right of Figure 8. Here, it should be noted that indium PI signals in the 9.1 eV image are quite low, and therefore the image shows evidence of incomplete subtraction of the SIMS background (i.e., the "matrix effect" that enhances the indium SIMS signal over the copper grid is clearly visible).

Copper PI signals integrated over the entire imaged area (not shown) exhibit the opposite trend, increasing in intensity as the light is tuned from 7.5 to 9.1 eV; however, the copper PI images at the two different photon energies do not clearly reflect this overall intensity change due to the low signal intensity of the copper PI (i.e., the fractional change in ionization probability is not large enough to be seen on a pixel-by-pixel level). Nevertheless, the wavelength dependence of individual PI peak intensities provides another parameter with which to verify mass assignments, which is particularly valuable for imaging mass spectrometry when hundreds of compounds exist within a given sample.

Conclusion

A keV bismuth cluster ion source is used together with tunable synchrotron VUV light to obtain PI mass spectra and PIE curves for sputtered neutrals from GaAs and Au surfaces from Bi^+, Bi_3^+, and Bi_3^{2+} primary ion bombardment. SIMS spectra are compared to the PI mass spectra, revealing the complementary nature of the two techniques. While the larger cluster species are more efficiently detected through the positive secondary ions, smaller species such as Au, Au_2, and As are detected with nearly the same intensity as SIMS, and As_2 is about an order of magnitude stronger through the neutral channel. Scans of the VUV light wavelength allow PIE curves to be obtained. No notable changes in the ionization thresholds for the various sputtered neutrals are observed with the use of the different primary ion beams, although comparisons with previous experimental adiabatic ionization energies reveal that the ionization thresholds for neutral clusters are typically shifted by ~0.3 eV toward lower photon energies, likely due to vibrational and rotational excitations.

The utility of tunable VUV light for high spatial resolution chemical imaging is also demonstrated with the analysis of a copper TEM grid embedded in indium. With reduced signal dependences on the local chemical environment and the additional selectivity afforded by the different photoionization cross sections of the sputtered surface species, threshold single photon PI with synchrotron VUV light promises to be a valuable technique for submicrometer imaging of chemically heterogeneous systems with mass spectrometry.

Acknowledgment. Several authors (S.R.L., K.R.W., M.A.) have benefitted enormously from highly productive collaborations and joint mentoring of students with George Schatz over the years. Special thanks go to Leonid Belau, Andreas Wucher, Joe Kazole, and Nicholas Winograd for their initial experimental work with synchrotron VUV postionization, to Monroe Thomas for his extensive help in coupling the TOF.SIMS 5 to the beamline, and to ION-TOF Inc. for their ongoing cooperation and support. We would also like to thank Oleg Kostko for taking measurements for our light wavelength calibrations, Hendrik Bluhm and Yaroslav Romanyuk for providing the samples on short notice, and Ricardo Metz for helpful discussions about vibrational temperatures. This work was supported by the Director, Office of Energy Research, Office of Basic Energy Sciences, and Chemical Sciences Division of the U.S. Department of Energy under contract no. DE-AC02-05CH11231. S.R.L. gratefully acknowledges the support of a Morris Belkin Visiting Professorship at the Weizmann Institute of Science.

References and Notes

(1) Quinn, P. K.; Bates, T. S.; Coffman, D. J.; Covert, D. S. *Atmos. Chem. Phys.* **2008**, *8*, 1029.
(2) Castner, D. G.; Ratner, B. D. *Surf. Sci.* **2002**, *500*, 28.
(3) Brown, W. L.; Sosnowski, M. *Nucl. Instrum. Methods Phys. Res., Sect. B* **1995**, *102*, 305.
(4) Garrison, B. J.; Postawa, Z. *Mass Spectrom. Rev.* **2008**, *27*, 289.
(5) Thompson, M. W. *Vacuum* **2002**, *66*, 99.
(6) McPhail, D. *J. Mater. Sci.* **2006**, *41*, 873.
(7) Kraft, M. L.; Weber, P. K.; Longo, M. L.; Hutcheon, I. D.; Boxer, S. G. *Science* **2006**, *313*, 1948.
(8) Colliver, T. L.; Brummel, C. L.; Pacholski, M. L.; Swanek, F. D.; Ewing, A. G.; Winograd, N. *Anal. Chem.* **1997**, *69*, 2225.
(9) Lechene, C. P.; Luyten, Y.; McMahon, G.; Distel, D. L. *Science* **2007**, *317*, 1563.
(10) Fletcher, J. S.; Lockyer, N. P.; Vaidyanathan, S.; Vickerman, J. C. *Anal. Chem.* **2007**, *79*, 2199.
(11) Ostrowski, S. G.; Van Bell, C. T.; Winograd, N.; Ewing, A. G. *Science* **2004**, *305*, 71.
(12) Kollmer, F.; Bourdos, N.; Kamischke, R.; Benninghoven, A. *Appl. Surf. Sci.* **2003**, *203*, 238.
(13) Wood, M.; Zhou, Y.; Brummel, C. L.; Winograd, N. *Anal. Chem.* **1994**, *66*, 2425.
(14) Wittig, A.; Arlinghaus, H. F.; Kriegeskotte, C.; Moss, R. L.; Appelman, K.; Schmid, K. W.; Sauerwein, W. A. G. *Mol. Cancer Ther.* **2008**, *7*, 1763.
(15) Mollers, R.; Terhorst, M.; Niehuis, E.; Benninghoven, A. *Org. Mass Spectrom.* **1992**, *27*, 1393.
(16) Muller, U.; Schittenhelm, M.; Schmittgens, R.; Helm, H. *Surf. Interface Anal.* **1999**, *27*, 904.
(17) Terhorst, M.; Mollers, R.; Niehuis, E.; Benninghoven, A. *Surf. Interface Anal.* **1992**, *18*, 824.
(18) Willey, K. F.; Vorsa, V.; Braun, R. M.; Winograd, N. *Rapid Commun. Mass Spectrom.* **1998**, *12*, 1253.
(19) Becker, C. H. *Fresenius' J. Anal. Chem* **1991**, *341*, 3.
(20) Wilson, K. R.; Jimenez-Cruz, M.; Nicolas, C.; Belau, L.; Leone, S. R.; Ahmed, M. *J. Phys. Chem. A* **2006**, *110*, 2106.
(21) Pan, Y.; Yin, H.; Zhang, T. C.; Guo, H. J.; Sheng, L. S.; Qi, F. *Rapid Commun. Mass Spectrom.* **2008**, *22*, 2515.
(22) Peterson, R. E.; Nair, A.; Dambach, S.; Arlinghaus, H. F.; Tyler, B. J. *Appl. Surf. Sci.* **2006**, *252*, 7006.
(23) Veryovkin, I. V.; Calaway, W. F.; Moore, J. F.; Pellin, M. J.; Lewellen, J. W.; Li, Y.; Milton, S. V.; King, B. V.; Petravic, M. *Appl. Surf. Sci.* **2004**, *231*−*232*, 962.
(24) Heimann, P. A.; Koike, M.; Hsu, C. W.; Blank, D.; Yang, X. M.; Suits, A. G.; Lee, Y. T.; Evans, M.; Ng, C. Y.; Flaim, C.; Padmore, H. A. *Rev. Sci. Instrum.* **1997**, *68*, 1945.

(25) Berkowitz, J. *Photoabsorption, Photoionization, and Photoelectron Spectroscopy*; Academic Press, Inc.: London, 1979.
(26) Marr, G. V.; Austin, J. M. *J. Phys. B: At. Mol. Opt. Phys.* **1969**, *2*, 107.
(27) Mazarov, P.; Samartsev, A. V.; Wucher, A. *Appl. Surf. Sci.* **2006**, *252*, 6452.
(28) Yamamura, Y.; Tawara, H. *At. Data Nucl. Data Tables* **1996**, *62*, 149.
(29) Yamamura, Y.; Itikawa, Y.; Itoh, N. *Angular Dependence of Sputtering Yield of Monoatomic Solids*; Institute of Plasma Physics: Nagoya University, 1983.
(30) Wucher, A. *Appl. Surf. Sci.* **2006**, *252*, 6482.
(31) Nagy, G.; Walker, A. V. *Int. J. Mass Spectrom.* **2007**, *262*, 144.
(32) Wucher, A.; Staudt, C.; Neukermans, S.; Janssens, E.; Vanhoutte, F.; Vandeweert, E.; Silverans, R. E.; Lievens, P. *New J. Phys.* **2008**, 10.
(33) Rothlisberger, U.; Schar, M.; Schumacher, E. *Z. Phys. D: At., Mol. Clust.* **1989**, *13*, 171.
(34) Yoo, R. K.; Ruscic, B.; Berkowitz, J. *J. Chem. Phys.* **1992**, *96*, 6696.
(35) Balasubramanian, K. *Chem. Rev.* **1990**, *90*, 93.
(36) Bhatia, K. S.; Jones, W. E. *Can. J. Phys.* **1971**, *49*, 1773.
(37) Moore, C. E. *Atomic Energy Levels*, circ. no. 467 ed.; National Bureau of Standards: Washington, DC, 1952; Vol. 2.
(38) Staudt, C.; Heinrich, R.; Wucher, A. *Nucl. Instrum. Methods Phys. Res., Sect. B* **2000**, *164*−*165*, 677.
(39) Moore, C. E. In *Atomic Energy Levels*, circ. no. 467 ed.; Commerce, U. S. D. o., Ed.; National Bureau of Standards: Washington, DC, 1958; Vol. 3, p 186.
(40) Cheeseman, M. A.; Eyler, J. R. *J. Phys. Chem.* **1992**, *96*, 1082.
(41) Das, K. K.; Balasubramanian, K. *J. Mol. Spectrosc.* **1990**, *140*, 280.
(42) Lee, H. M.; Ge, M. F.; Sahu, B. R.; Tarakeshwar, P.; Kim, K. S. *J. Phys. Chem. B* **2003**, *107*, 9994.
(43) Wang, J.; Wang, G.; Zhao, J. *Phys. Rev. B* **2002**, *66*, 035418.
(44) Jackschath, C.; Rabin, I.; Schulze, W. *Ber. Bunsen-Ges. Phys. Chem.* **1992**, *96*, 1200.
(45) Wucher, A. *Phys. Rev. B* **1994**, *49*, 2012.
(46) Karamatskos, N.; Muller, M.; Schmidt, M.; Zimmermann, P. *J. Phys. B: At. Mol. Opt. Phys.* **1984**, *17*, L341.
(47) Platt, J. R.; Sawyer, R. A. *Phys. Rev.* **1941**, *60*, 866.
(48) Ray, A. K. *Comput. Mater. Sci.* **2002**, *25*, 279.

JP810408V